Brehme, M., Regenspurg, S., Leary, P., Bulut, F., Milsch, H., Petrauskas, S., Valickas, R., Blöcher, G. (2018): Injection-Triggered Occlusion of Flow Pathways in Geothermal Operations. - *Geofluids*, *2018*, pp. 1—14.

DOI: http://doi.org/10.1155/2018/4694829

Hindawi
Geofluids
Volume 2018, Article ID 4694829, 14 pages
https://doi.org/10.1155/2018/4694829

Research Article

Injection-Triggered Occlusion of Flow Pathways in Geothermal Operations

Maren Brehme,[1] **Simona Regenspurg**,[1] **Peter Leary**,[2] **Fatih Bulut**,[3] **Harald Milsch**,[1] **Sigitas Petrauskas**,[4] **Robertas Valickas**,[4] **and Guido Blöcher**[1]

[1]*Helmholtz Centre Potsdam-GFZ German Research Centre for Geosciences, Geothermal Energy Systems, Telegrafenberg, 14473 Potsdam, Germany*
[2]*Advanced Seismic Instrument & Research, 1311 Waterside, Dallas, TX 75218-4475, USA*
[3]*Department of Geodesy, Kandilli Observatory and Earthquake Research Institute, Bogazici University, 34684 Istanbul, Turkey*
[4]*UAB GEOTERMA, Lypkių g. 17, LT-94100 Klaipėda, Lithuania*

Correspondence should be addressed to Maren Brehme; brehme@gfz-potsdam.de

Received 8 February 2018; Accepted 22 May 2018; Published 5 July 2018

Academic Editor: Julie K. Pearce

Reasons for injectivity decline were investigated in a low-enthalpy geothermal aquifer in Klaipeda (Lithuania). It is one of the study sites within the DESTRESS project, which demonstrates different stimulation techniques in geothermal reservoirs. Due to low injectivity, production rates from the Lithuanian field are currently reduced, which lead to negative commercial implications for the site. Productivity from the same wells is measured to be 40 times higher. Injectivity decline in aquifers is often related to clogging processes in spatially correlated highly permeable structures, which control the main flow volume. We subdivided clogging processes into (1) physical, (2) chemical, and (3) biological processes and studied them by analyzing fluid and solid samples as well as operational data. The methods we used are fluid and solid analyses in situ, in the laboratory and in experimental setups, statistical interpretation, and numerical modeling. Our results show that the spatially correlating nature of permeable structures is responsible for exponentially decreasing injectivity because few highly permeable zones clog rapidly by intruded particles. In particular, field operations cause changes of the physical, chemical, and biological processes in the aquifer. Mineral precipitation and corrosion are the main chemical processes observed at our site. Microbial activity causes biofilm while fines migration is caused by changes in physical boundary conditions. Moreover, these processes can affect each other and generate further reactions, for example, microbial activity triggers corrosion in surface pipelines.

1. Introduction

Fluid flow in geological media occurs at the grain scale in spatially correlated poroperm structures where a few high permeable flow paths control the main flow volume [1]. These highly permeable flow paths can be clogged by small particles due to physical, chemical, and biological processes. When these processes happen near a geothermal injection well, net fluid flow decreases quickly, leading to negative commercial implications for the site. In this paper, we study clogging processes in a low-enthalpy geothermal aquifer in Lithuania using fluid and solid analysis as well as operational data.

Clogging processes in geological media are often related to field operations or artificially intruded materials and can be of physical, chemical, or biological nature. However, which processes are triggered by field operations, how the different processes interact, and the subsequent implications for flow paths are not yet fully understood.

In this study, we subdivided clogging processes as follows: (1) Physical processes refer to the structure and hydraulic properties of the aquifer. (2) Chemical processes represent mainly the composition of fluids and solids as well as chemical reactions between them, for example, dissolution and precipitation. (3) Biological processes summarize reactions mainly driven by bacterial activity, for example, sulfate

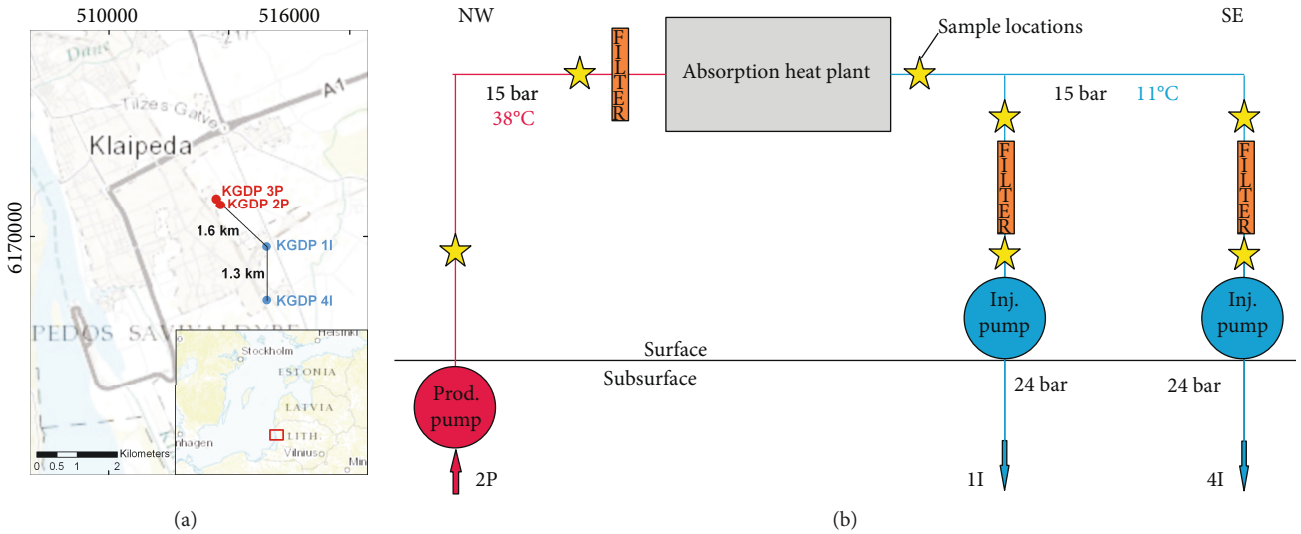

Figure 1: Location (a) and setup (b) of the Klaipeda geothermal demonstration plant. Including operational parameters of the plant and sample locations (yellow stars).

reduction or biofilm formation. The process types might not only play an individual role, but also be coupled in the geological media. These processes are usually investigated by laboratory experiments and numerical modeling.

Laboratory experiments focus in general on a single process, that is, hydraulic properties [2], scaling effects [3, 4], and microbial activity [5]. Here, hydraulic properties and physical behavior of rocks are important to characterize fluid flow pathways and therefore to design hydraulic stimulation experiments [6, 7]. Chemical and biological reactions are investigated to avoid scaling and biofilm-induced permeability reduction through scaling and biofilms [8, 9].

Modeling approaches are used to mostly investigate coupled processes governing subsurface fluid flow in geothermal reservoirs [10, 11]. Their primary objective is to ensure sustainable use of geothermal reservoirs [12–14]. Previous studies show that an integrated analysis of flow processes is essential for understanding controls of fluid flow [15].

Nevertheless, these processes can also be understood inherently from in situ field data. Basic analysis of fluids and solids can be interpreted to explain fundamental parameters governing the fluid flow in the reservoir (e.g., [16]).

In this paper, we study physical, chemical, and biological parameters affecting subsurface fluid flow in a low-enthalpy geothermal aquifer in Klaipeda, Lithuania, using fluid and solid analyses as well as operational data. Our results show that field data already allow us elaborating on subsurface processes. In particular, we investigate interaction between physical, chemical, and biological processes to understand occlusion of fluid pathways. The results show that the nature of spatially correlating permeable structures is the main reason for the observed exponentially declining injectivity.

This study is carried out in the framework of the EU-funded project DESTRESS (Demonstration of soft stimulation techniques of geothermal reservoirs). In this project, sites in different geological settings are studied in order to afterwards demonstrate the best stimulation technique. The key goal of DESTRESS is to demonstrate the success of stimulation treatments in long-term enhanced productivities and injectivities.

2. Site, Setup, and Precondition

Our test site, the Klaipeda Geothermal Demonstration Plant (KGDP hereafter), is located south of the city center of Klaipeda (Lithuania) in the free economic zone (Figure 1(a)). The site was selected for geothermal operation during the feasibility study of the Baltic Geothermal Energy Project, which was running from 1992 to 1994. Drilling started in 1997, and the geothermal plant was commissioned in 2000. Originally, the total geothermal capacity of the power plant was 17 MWth (thermal energy) which covers ~20% of the heating demand of the city of Klaipeda (Zinevicius et al., [17]).

The KGDP wells target a lower Devonian sandstone aquifer at 1.1 km depth. The water is 36°C warm, highly saline (108 g/l) and found to be one of the oldest in the world, dated to 1.16 Ma [18]. The geothermal gradient is 34.5°C/km. Water is further heated up by gas boilers to 70°C, and the absorbed heat is delivered to the local heating system of the city. Since 2013, the site usually runs from October to April depending on seasonal heat demand. Out of four wells, one well currently serves as production well, and two others serve as injection wells (Figure 1(b)). The fourth was in use as production well but has been abandoned due to reduced overall flow rates within the geothermal cycle. The theoretical flow rate within the geothermal cycle is 800 m^3/h. However, it was reduced to 200 m^3/h because of low performance of injection wells. Production and injection wells are located on a NW-SE striking profile and in ~1.5 km distance. The wells are cased and equipped with slotted liners in 9 5/8″. Filter bags are installed at the surface of production wells to remove solid particles, which are flushed during

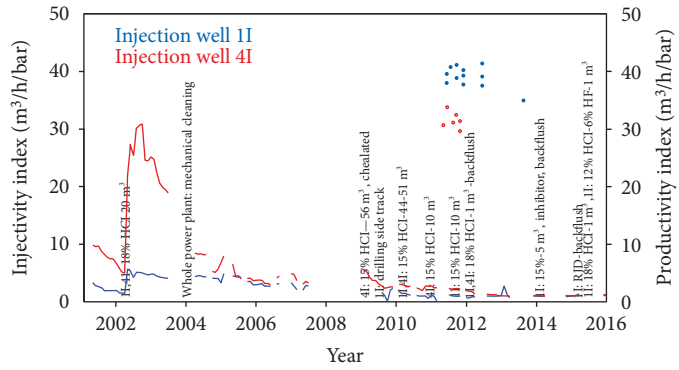

FIGURE 2: Injectivity and productivity indices of two injection wells including stimulation treatments between 2001 and 2016. Lines show daily measurements of injectivity index; dots show single production tests in well 1I (blue) and well 4I (red).

production of reservoir fluid. Similar filters are placed right before injection.

In 2001, the initial injectivities were 10 m^3/h/bar (injection well 4I) and 3 m^3/h/bar (injection well 1I). Directly after start of fluid production, injectivities began to decrease. A first acidation attempt in 2002 resulted in well performance increase from 5 to 31 m^3/h/bar (4I) and 1 to 6 m^3/h/bar (1I) (Figure 2). Since then, injectivities were constantly decreasing to currently 1 m^3/h/bar in both wells. Several attempts have been undertaken to overcome the low injectivities. Treatments include acidation, reverse pumping, use of bactericides, radial jet drilling, and drilling a side track in one of the injection wells. However, treatments achieved only short-term improvements and at most 1.3 (1I) and 2.7 m^3/h/bar (4I) absolute injectivity increase (Figure 2). The strongest decrease was observed in 2003, when massive gypsum precipitations forced the power plant to be shut down. At that time, the surface installations had to be completely cleaned in addition to the wells before starting up the operation again. Since then, a sodium phosphonate-based gypsum inhibitor is used and precipitation is successfully avoided.

Meanwhile, in the same wells, measured productivities are 40 times higher than measured injectivities (Figure 2). Theoretical calculation of aquifer productivity gives rather a higher value of 60 m^3/h/bar. Thus, the aquifer is theoretically capable of higher flow rates. This large difference between productivity and injectivity in the same wells indicate a direction-dependent fluid barrier and will be discussed later.

3. Methods and Data

The database compiled during this study consists of water and gas samples from different points of the thermal loop, drill cores, and filter residual from different wells, a bailer sample from well 1I additionally to historical operational data. Water, gas, core, and filter residual samples have been analyzed using various methods in order to understand physical, chemical, and biological processes in the Klaipeda geothermal reservoir. The database and the analysis are further described as follows:

3.1. Fluid Analysis. Physicochemical parameters of water have been measured after sampling seven locations directly at the site in March and July 2016 (Figure 1). Chemical composition of water samples has been analyzed for its chemical composition in the following procedure: water samples were collected in clean polyethylene bottles, each thoroughly rinsed three times with water to be sampled after pumping for several hours. At each sample point, two 50 mL samples were filtered using 0.45 μm cellulose acetate filter paper. For cation analyses, samples were acidified with HCl. All samples were brought to the geochemical laboratories of the GFZ Potsdam and analyzed with regard to major anions and cations. For details on measurement techniques, refer to Brehme et al. [19] and Brehme et al. [20].

Artificial reservoir water has been produced to test filter material from the site on release of organic material. The filter material has been exposed to the artificial reservoir water in a leaching experiment, where the water circulated around the unused filter material for one week. Water samples were taken in regular time intervals and tested on dissolved organic carbon (DOC). Dissolved organic carbon has been determined also in natural reservoir water with a nondispersive infrared detector.

Gas samples have been taken at the production well 2P and at the injection well 4I. The composition has been analyzed using gas chromatography in laboratories at GFZ Potsdam.

Microbiological analysis focus on microbial abundance and community structure in water samples taken in March 2016 [21]. The OTU (operational taxonomic unit) has been used to analyze the bacterial community composition. Its diversity has been determined by the Simpson and Shannon index.

Abundant bacteria and archaea have been distinguished, and their abundance influencing factors have been described. Furthermore, cell counting has been realized in the sampled water.

3.2. Solid-Phase Analysis. A total of 18 core samples from reservoir depth in injection well 1I and neighboring wells, a bailer sample from injection well 1I taken in 2014 and filter residual taken in 2016 from filters at production and

injection sites (Figure 1), have been analyzed optically and on its mineralogical composition using X-ray powder diffraction. Samples have been handled following the procedure in Deon et al. [22]: first, samples have been crushed and sieved to obtain the 63 μm fraction. XRD patterns were recorded in transmission using a fully automated STOE STADI P diffractometer at GFZ Potsdam. The diffractograms were refined with the EXPGUI-GSAS software.

Filter residual and a core sample from injection well 1I have been additionally analyzed on carbon, nitrogen, and sulfur content (CNS). Samples are heated and converted into its gaseous components before measuring following the Dumas method [23]. Porosity of core sample from injection well has been determined by mercury injection porosimetry for effective porosity measurements. Different permeability models have been applied to the dominant pore size fraction to determine the permeability.

Sampled water has been further tested on floating particles and their size at different locations of the fluid cycle (Figure 1). 10 l of water has been pumped through a 0.1 μm filter. Filter residual has been analyzed versus particle size.

3.3. Fluid-Solid Interaction Modelling. Chemical data from fluids and solids have been combined in a hydrochemical model setup in PHREEQC using the phreeqc.dat database. The code is able to calculate potential precipitation and dissolution reactions within 0 to 200°C and 1 to 1000 atm based on the Peng-Robinson state equation [19]. Precipitation and dissolution reactions result from fluid-solid interaction and depend on temperature and pressure changes.

Furthermore, hydrochemical data have been analyzed by cross correlation to investigate similarity of chemical measurements between different elements. Cluster analysis is performed to objectively sort the elements into subgroups using cross correlation coefficients as the distance metric.

3.4. Operational and Historical Data Analysis. Operational and historical data from 2001 to 2017 have been conclusively analyzed focusing on reservoir processes and subsurface fluid flow structures. Here, injectivity and productivity data identify time-dependent changes in the subsurface flow system.

3.5. Wellbore Statistics and Modelling. Additionally, well logs have been investigated to characterize natural pore connectivity structures. Generally, pore connectivity structures are characterized by a single spatial correlation process on a scale range of cm to km. The crustal spatial correlation process is seen as 1/fn power-law scaling of well-log Fourier power spectra [24]. f is the spatial frequency and varies over five decades from 1/km to 1/cm, and n is the scaling exponent. Power-law scaling spatial correlation means that pore connectivity and associated permeable structures cannot be meaningfully averaged within or across geological layers.

In order to show the effect of spatial correlation on wellbore flow, a 2D wellbore-centric radial injectivity flow decline modelling was set up. Scenarios in spatially correlated and spatially uncorrelated flow structures were simulated. The permeability field $\kappa(x, y)$ is determined by the flow-layer porosity field $\varphi(x, y)$, $\kappa(x, y) = \kappa_0 * \exp(\alpha\varphi(x, y))$, where α is constant. Results show the depth of particle infiltration in different environments and related injectivity decline curves. Details are given in the Appendix.

4. Results

4.1. Physical Processes. There are four wells at the Klaipeda geothermal power plant targeting a lower Devonian sandstone aquifer at 1.1 km depth (Figure 3). Injection well 1I, drilled in September/October 1997, has a final depth of 1130 m below surface. In May 2009, a side track was deviated with 3.5° from 897 m to a final depth of 1116 m. Injection well 4I was drilled in October 1998 as a straight well 1.3 km south of well 1I down to a final depth of 1129 m below surface. Production well 3P was drilled in November 1997 to a final depth of 1225 m below surface while production well 2P was finished in December 1997 at a final depth of 1128 m below surface.

Several hydraulic tests were performed between 1997 and 2008. These include two air lift tests (1I and 4I), two flow profiling while injection, and one pump test to evaluate the interference between 1I and 4I. Most suitable data for performing well test analysis were available from an air lift test performed in 1998. This air lift test was performed in well 4I. 4.5 hours of pumping with different flow rates having an average of 54.1 m^3/h was followed by 5.5 hours of pressure buildup. From the production phase, a 50 m^3/h/bar productivity and 1.1 bar corresponding drawdown were estimated at the end of production based on the average flow rate. The buildup data were treated analytically and numerically. The numerical results performed with Saphir NL (Kappa 1990–2008) indicate a transmissibility of T = 218 Dm which is equivalent to a permeability of 2.5 D considering an aquifer thickness of 86 m. The analytical estimation of the reservoir transmissibility was performed by decline curve analysis taking into account the superposition principle and assuming infinite acting radial flow. A transmissibility of 79 Dm and a corresponding permeability of 2.1 D were obtained. These results are in good agreement with hydraulic aquifer properties reported by the well testing company Dansk Olie OG Naturgas A/S.

Wells are located within the Baltic cratonic sedimentary basin, which consists of weakly tectonized sediments (Sliaupa 2016, unpublished report). The wells first cut quaternary glacial deposits and Triassic gypsum-bearing clays until 280 m below surface, before they hit 50 m thick Permian limestones. Underlying sequences are of Devonian age, which make up 70% of the well formations. 300 m Devonian limestones and dolomites overlay interbedded sandstones and dolomitic sandstones. Tight clays and silt cover the aquifer sequence above 970 m. At aquifer depth (~975–1130 m), sandstones interbed with clay layers; some of which are up to 20 m thick.

The aquifer sections of all wells are equipped with 9 5/8″ liners including screens with 0.008″ wire spacing at the depth of sandstone layers. Production wells and well 4I are additionally supplied with a 40/60 mesh gravel (grain size: 0.25–0.42 mm, medium sand). Well 1I has an open hole section between the depths of 1082 and 1116 m.

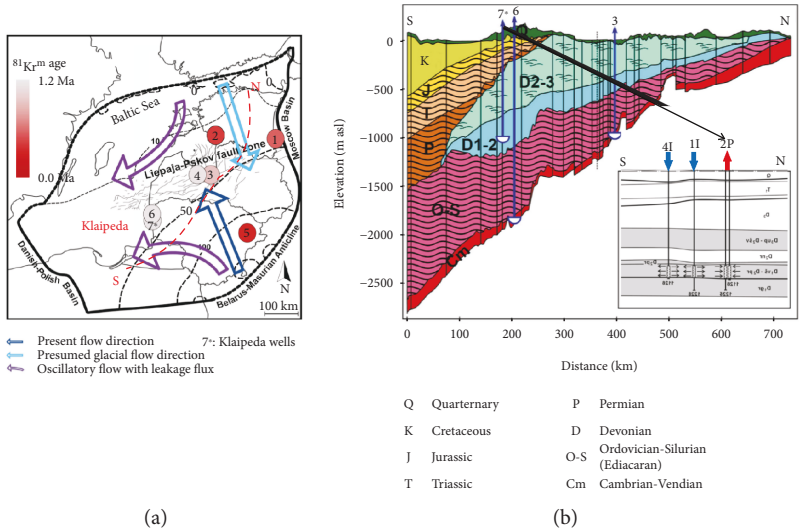

(a) (b)

FIGURE 3: (a) Groundwater flow direction and age in the Baltic Sea area after Gerber et al. [18]. (b) Geological cross section and well location of the Klaipeda site, modified after Gerber et al. [18] and Zinevicius et al. [17].

The gravel pack at production site does not prevent reservoir rock material to be flushed into the thermal loop. Filter bags at the surface contain aquifer rock material from the produced fluid. 30% of the captured material is made out of middle to fine sand and clays; the rest is magnetite and corroded casing.

Aquifer rock has been sampled by coring the sidetrack in well 1I. Cores from sandstone layers show well-sorted middle sand with grains that are poorly cemented. Cores from mudstone layers consist of clayey and silty particles (1–62 μm). Analysis of sandstone samples by mercury injection porosimetry showed a reproducible overall pore size distribution and a porosity of about 26%. 85% of the total pore volume is made up of pores with a size between 3 and 40 μm, where the pore size class around 20 μm dominates and accounts for about 25% in total. The remainder (15% by volume) comprises a broad range of pore throat radii between less 3 μm and about 4 nm. A Carman-Kozeny-type permeability model applied to the dominant pore size fraction (3 to 40 μm) indicates a rock permeability of around 6 D. For the same formation, Sliaupa (2016, unpublished report) indicates porosities of 10–30% and permeabilities between 2.2 and 4.9 D.

Water filter analysis shows that the main particle size ranges from 4 to 40 μm. These particles are floating in the water and pumped into injection wells even behind installed 1 μm filters. Floating particles have the same size range as pores leading to a further clogging risk.

The structural setup of the aquifer is dominated by horizontal layering of Quaternary, Triassic, Permian, and Devonian sediments (Figure 3). Highly permeable zones alternate with tighter layers in the major aquifer flow structure. No major faults were detected in seismic profiles. Therefore, a combination of fractures and cracked grain-scale cement bonds is expected to locally control the fluid flow in the aquifer. As permeable structures are void spaces for fluids, they can be easily observed in well logs which record fluid characteristics. The spatial distribution is described by the expression S(f)~1/fn where S(f) is the Fourier power spectrum of a well log, f is the spatial frequency and varies over five decades from 1/km to 1/cm, and n is the scaling exponent. Exponent n would be 0, if permeable structures are uncorrelated, and 2, if permeable structures are strongly linked to geological layering. For spatially uncorrelated structures, as observed in the Earth's crust, n~1 [24].

In Klaipeda, the porosity-log spectral power-law scaling exponents are determined to be $n = 0.93$ for the porosity-log of well 3P, for well 1I it is $n = 1.2$, and for well 4I it is $n = 1.1$ (Figure 4). The porosity sequences with 1/k (1/f) spatial fluctuation power-law scaling show that the spatial correlation nature of the local crustal flow structures is neither uncorrelated Gaussian fluctuations (spectral scaling exponent ~0) nor strongly correlated spatial scaling due to geological layering (spectral scaling exponent ~2). With reference to injectivity flow modelling below, it can be noted that the Figure 4 1/k (1/f) spatial correlations also apply along the lateral extent of the major flow system aquifer.

4.2. Chemical Processes. The chemical composition of water has been analyzed since 1997. Recent measurements for this study in 2016 show that it is a highly saline brine with an electrical conductivity of ~129 mS/cm, total dissolved solids of 93 g/l, and a pH of ~6.6. The produced water has a temperature of 36°C and is injected at 11°C. Main components of the water are Cl, Na, Ca, Mg, SO_4, and Br. Also, Sr and HCO_3 have increased concentrations (Table 1).

Long-term observation of water composition shows that concentrations of several elements are changing since the start of production. At a production site, the most prominent changes are in HCO_3, Si, and Li concentrations. At an injection site, HCO_3, Si, Fe, and Li concentrations change most. Generally, HCO_3, Fe, and Mn increased at the production site and injection site by 18–40%. Si and Li principally decreased by 30–34%. Only at well 4I, also HCO_3 decreased

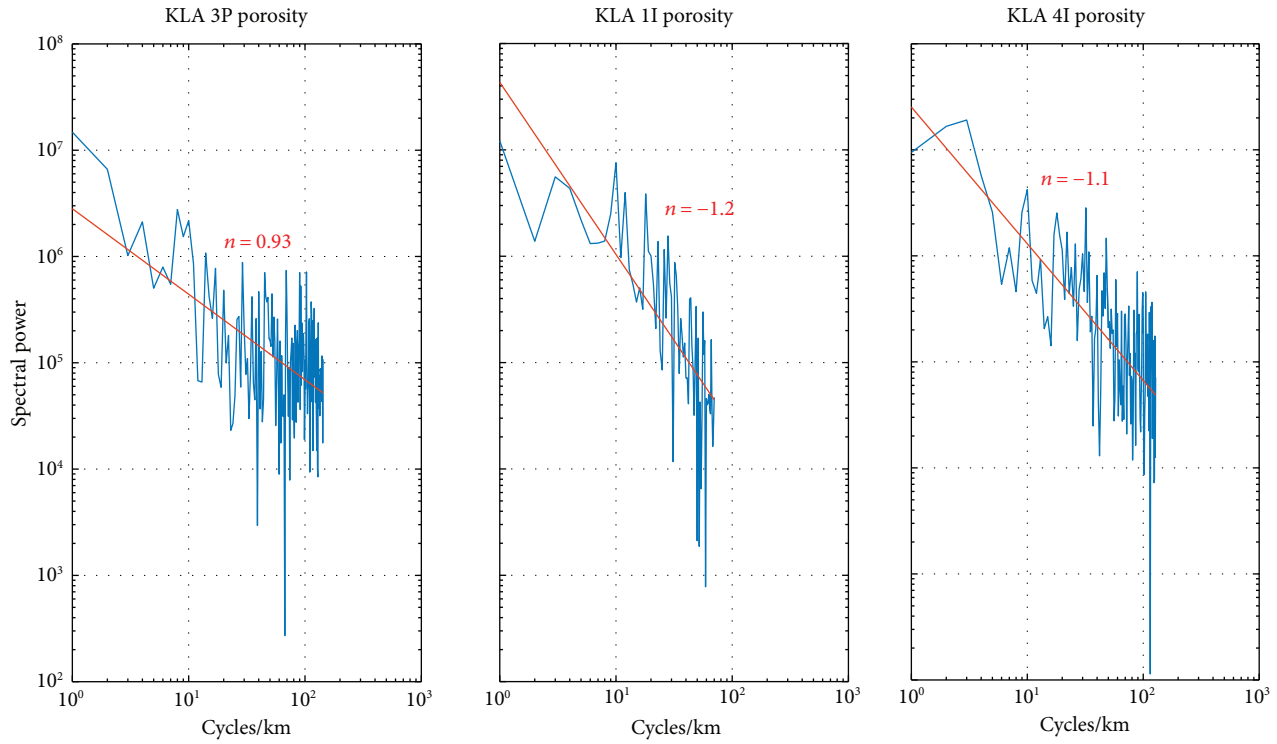

Figure 4: Fourier power spectra of porosity well logs for Klaipeda wells 3P, 1I, and 4I.

by 31%. Additionally, a single strong signal (−50%) is observed in K concentrations at well 4I.

Additionally, the produced fluid in the Klaipeda production wells contains at 39°C a total amount of 4.5% gas under 15 bar pressure (GTN 2011, unpublished report). The main composition of the gas content consists of N_2 (80.1%), CO_2 (19.8%), few CH_4 (0.024%), and H_2S (0.0005%).

The aquifer formation is an interlayering of sandstones, siltstones, and mudstones of lower Devonian age (>400 Ma). The formation has been sampled and mineralogically analyzed from the Klaipeda well 1I and several nearby wells. The results show that typical sandstone samples are composed of quartz, calcite, dolomite, and some biotite. Whereas mudstone generally consists of quartz, muscovite, biotite, pyrite, kaolinite, illite, and some hematite.

Solid material transported from the aquifer well casing or surface pipelines is accumulated in filters right after production and directly before injection. Beside sandstone and mudstone, gypsum minerals were identified. 60% of the solids can be related to corrosion occurring both in the production well and before injection. Corrosion products form small ferromagnetic plates of 1–10 mm in diameter. They are mainly composed of magnesioferrite, spinelloid, and lepidocrocite. Similarly, the bailer sample from well 1I yields a mixture of sandstone, mudstone, and corrosion minerals.

Corrosion processes are confirmed also by the observation of relatively high total concentrations of Mn, Fe, and Si in water. Mn, Fe, and Si are components of "4140" or "L80" steel which is used as material in wells and pipes. Additionally, these element concentrations positively correlate with each other at all locations of the thermal cycle (Figure 5). That means that increasing Mn concentration (probably from dissolution processes) implies increased Fe and Si concentration. Overall, Mn and Fe concentrations increase from production to injection site indicating a higher or accumulating chemical reactivity towards the injection site.

The interaction of fluids with solids also leads to leaching and precipitation processes in the aquifer. This process can be observed in correlation of specific element concentrations in water (Figure 5). Positive correlation and increasing concentrations indicate dissolution of minerals; decreasing total concentrations show precipitation of minerals. Hence, the correlation of HCO_3, Ca, and Mg concentrations suggests leaching of dolomite and calcite from reservoir rocks probably by mechanical force.

Furthermore, the strength of correlation between different chemical elements can be further analyzed with a hierarchical clustering tree based on correlation-derived Euclidean distances (Figure 5(b)). Element families with high cross-correlation show similar response to chemical reactions. The lower the Euclidean distance (y-axis in Figure 5(b)), the higher the strength of correlation. Three main groups have been distinguished which also reflect the above-described processes. B, Si, Fe, Li, Ba, and Mn correlate while Mg, HCO_3, Ca, and Br build another group. Also Cl, SO_4, Na, F, K, and Sr show similar chemical behavior. The first group represents corrosion of pipelines and therefore increases in Mn, Fe, and Si concentration. The second group shows dissolution of reservoir minerals and therefore correlation of HCO_3 with Mg and Ca. Elements of the third group are responsible for the high salinity and therefore correlate with the electrical conductivity. The highest reverse correlations

Table 1: Historical and recently hydrochemical composition of water sampled in 2016 at different locations at the Klaipeda geothermal site, see Figure 1 (Wolfgramm 2008 and 2010, unpublished reports by GTN Neubrandenburg). Italic numbers are years.

Sample		KGDP-2P		KGDP-1I			KGDP-4I		
Well type		Production well since 1997		Injection well since 1997			Injection well since 1998		
Location		Before filter	Before filter	Before filter	Before filter	After filter	Before filter	Before filter	After filter
Sample date		*July 2001*	*March 2016*	*1997*	*March 2016*	*April 2016*	*1998*	*April 2016*	*April 2016*
pH	—	6.3	6.55	5.9	6.63	6.63	6.2	6.54	6.49
Electrical conductivity	(μS/cm)	134,134	125,300	129,920	130,900	129,500	137,808	130,200	129,400
Total dissolved solids (TDS)	(mg/l)	95,810	89,801	92,800	93,814	92,811	98,434	93,312	92,739
T	(°C)	37.8	36.4	17.6 *(2001)*	10.1	12.7	17.2 *(2001)*	11.7	13.3
Redox	(mV)	48	−133	−6 *(2001)*	−94	−56.2	−9 *(2001)*	−4.2	−45.5
O_2		0.1 *(2010)*	0.45		0.11	2.3	0.1 *(2010)*	0.55	0.38
HCO_3		55	85.4	112	85.4	85.4	52	85.4	91.5
F		0.25 *(2010)*	0.38		0.37	0.35	0.2 *(2010)*	0.34	0.36
Cl		58,400	56498.4	56,000	56009.9	54253.5	61,250	54899.3	53568.1
Br			355.9		333.6	347		353.7	363
NO_3			<0.6		<0.6	<0.6	<1 *(2010)*	<0.6	<0.6
SO_4		1830	1733.1	1910	1735.5	1742.4	1756	1707.7	1650.5
Na		25,000	24,299	24,550	24,249	24,022	25,150	24,481	24,225
K		600	616	611	621	619	915	607	620
Ca	(mg/l)	7600	7558	6820	7500	7532	9100	7484	7506
Mg		2250	2375	2140	2344	2359	2700 *(1999)*	2355	2358
Fe		14	17	14 *(2001)*	18	18	14 *(2001)*	18	18
Mn		0.82	1	0.82 *(2001)*	1	1	0.82 *(2001)*	1	1
Li		4.53 *(2010)*	3.4		3.7	3.5	4.41 *(2010)*	3.4	3.3
B		10.4 *(2010)*	9.3		9.8	9.6	10.1 *(2010)*	9.3	9.1
Si		6.3 *(2010)*	4.7		4.9	4.9	6.3 *(2010)*	4.7	4.7
Sr		140	165	145	167	167	145 *(1999)*	163	167
Ba			0.19		0.2	0.19	0.21 *(2010)*	0.19	0.18
Al		0.017 *(2010)*	0.019 *(2015)*				0.018 *(2010)*		

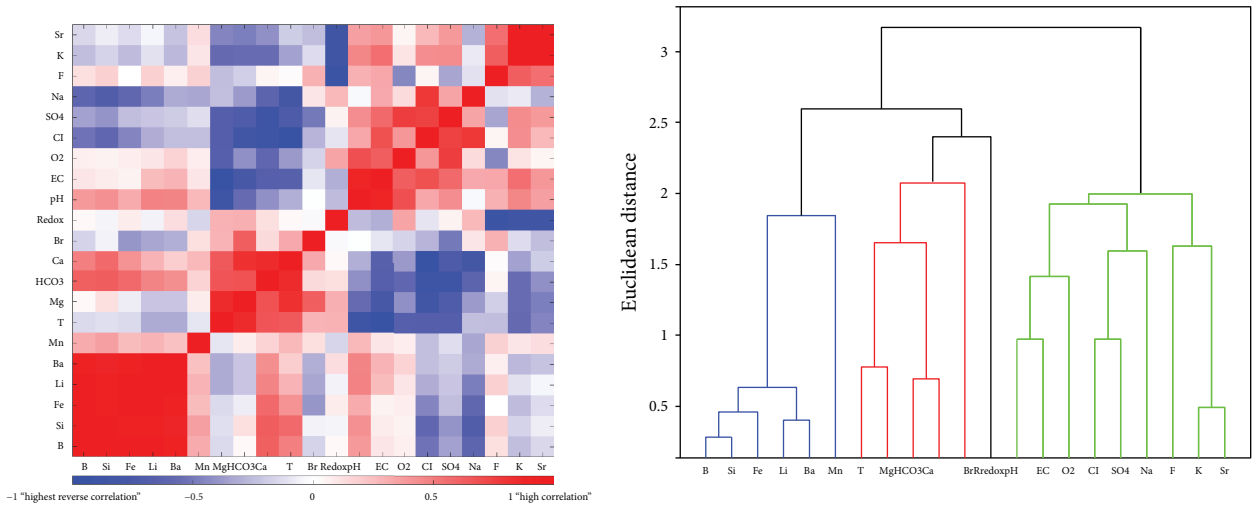

(a) (b)

Figure 5: (a) Correlation of chemical elements in the geothermal fluid (−1: highest reverse correlation, 0: no correlation, and 1: highest correlation); (b) strength of correlation shown by subgrouping of chemical elements using cluster analysis based on cross-correlation-derived Euclidian distances. EC: electrical conductivity.

Table 2: Results of hydrochemical modeling. Saturation index shows the possibility of precipitation of indicated minerals in the respective scenario (2P: production site, 1I: injection site, and equ.: equilibrium).

Supersaturated minerals		2P in equ. with rock	1I in equ. with rock	1I in equ. with rock + acidation	1I in equ. with rock + acidation + drill mud
Mineral phase	Mineral formula	Saturation index	Saturation index	Saturation index	Saturation index
Albite	$NaAlSi_3O_8$	4.99	4.99	4.99	5.45
Anhydrite	$CaSO_4$	0.54	0.09	0.09	0.61
Anorthite	$CaAl_2Si_2O_8$	8.43	7.55	7.54	8.39
Barite	$BaSO_4$	0.33	0.59	0.59	0.87
Ca-Montmorillonite	$Ca_{0.165}Al_{2.33}Si_{3.67}O_{10}(OH)_2$	0.06	−0.17	−0.17	0
Celestite	$SrSO_4$	0.71	0.07	0.07	0.19
Chlorite (14A)	$Mg_5Al_2Si_3O_{10}(OH)_8$	64.45	65.39	65.38	69.24
Chrysotile	$Mg_3Si_2O_5(OH)_4$	37.16	38.34	38.33	40.63
Gypsum	$CaSO_4{:}2H_2O$	0.58	0.22	0.22	0.68
Hausmannite	Mn_3O_4	4.11	3.69	3.68	5.56
Pyrochroite	$Mn(OH)_2$	4.04	5.61	5.6	6.22
Sepiolite	$Mg_2Si_3O_{7.5}OH{:}3H_2O$	23.42	24.93	24.92	26.39
Sepiolite(d)	$Mg_2Si_3O_{7.5}OH{:}3H_2O$	20.23	22.37	22.36	23.82
Talc	$Mg_3Si_4O_{10}(OH)_2$	40.34	41.02	41.01	43.34

occur for elements which cannot form chemical reactions or build minerals in this environment.

Fluid-rock interaction was additionally assessed by hydrochemical modeling. The oversaturation of specific minerals is an indicator for possible precipitation. It was calculated under different circumstances (production/injection) and additionally considers the effect of acidation and remaining drill mud (mainly montmorillonite) at injection site (Table 2).

The results from hydrochemical modeling with PHREEQC (see "Methods and Data") show that at production site several silica (albite, anorthite) including clays (chlorite, montmorillonite, and talc) and different sulfate minerals (celestite, gypsum, and barite) are oversaturated. However, gypsum inhibitor is used since 2004 and precipitation is successfully avoided.

According to hydrochemical modeling, similar minerals are oversaturated at injection site. When modelling the effect of acidation on these oversaturated minerals, it results in slightly less clay precipitation. However, the overall effect is hardly measurable. In contrast, including the remaining drill mud into the model results in clearly more precipitation of Mg-silicates (chlorite, chrysotile, and sepiolite) and sulfate minerals (gypsum, celestite, and barite).

4.3. Biological Processes. Former studies at the Klaipeda geothermal site from 2008 show that there were different organic populations at production and injection sites. Sulfate-reducing bacteria were mostly detected at the production site. The amount of Archaea was nearly same at production and injection sites. In 2008, the total amount of Archaea and sulfate-reducing bacteria was lower at the injection site ($3.2^{*}10^{4}$ cells/ml) than at the production site ($5.5^{*}10^{4}$ cells/ml). Recent cell counting suggests that the number of cells/ml has generally decreased during the last 8 years and is lower at the production site ($3.04^{*}10^{2}$ cells/ml) compared to the injection site ($8.58^{*}10^{2}$ cells/ml).

A study on microbial activity and community structure shows that 89.9% of the community is composed of bacteria and only 1.1% of Archaea [21]. The Simpson and Shannon index describes the microbial diversity which is very high in the Klaipeda aquifer (4.32/0.97). Further investigations show that the microbial diversity is mainly influenced by pH. A pH of 6.6 defines the aquifer as slightly acidic with a moderate temperature of 36°C. This is an optimal environment for the growth of Desulfobacca, a sulfate-reducing bacterium detected in the sampled water. Its existence confirms the anaerobic conditions and high sulfate concentration in water. The detected high evenness (0.29) can be explained by seclusion of the aquifer [21].

Bacteria are fed by organic material, nitrogen, or sulfur in fluids and solids. Therefore, increased CNS content could be an indicator for microbial activity. Especially, high S concentrations are an indicator for sulfate-reducing bacteria. However, it is probably also increased due to high gypsum content. At the Klaipeda site, the CNS content in filter residual is higher than the reservoir rock (Table 3). More precisely, the highest C, N, and S concentrations occur in filter residual at the injection site. This suggests that microbial activity develops mainly within the surface infrastructure of the power plant and that calcite and gypsum mineral precipitation occurs in the surface water cycle.

Dissolved organic carbon (DOC) values have been measured at production and injection sites. Results indicate DOC values of 1.6 to 2.4 mg C/l geothermal water. The values are increased at the injection site, especially behind filters.

DOC has also been measured during an experiment with artificial geothermal fluid that reproduces the natural composition. The artificial geothermal fluid was circulated around an unused filter from the Klaipeda site for five days, to test leaching of DOC from the filter into the water. DOC concentration measured at the end of the experiment was 4.0 mg C/l.

Table 3: CNS concentrations in core material and filter residual from the production (2P) site and injection (1I) site.

Name	% N	% C	% S
KLA_1I filter	0.30	3.26	9.85
KLA_2P filter	0.06	0.72	1.73
KLA_1I core	0.00	0.05	0.64

5. Discussion

Geothermal flow systems are highly sensitive environments defined by physical, chemical, and biological boundary conditions operating in geological time scales. However, field operations introduce agents that can more rapidly change the natural environment. Due to the sensitivity, small changes can lead to a significant negative influence on fluid flow near injection wellbores and hence sustainability of the geothermal system.

We illustrate this in reference to Figure 4, by considering that particles injected into an aquifer with high pressure can alter the natural flow pathways in the aquifer in long term. Here, the main alteration effect is the changes in grain-scale connectivity. These changes in the aquifer flow pathways can be induced by chemical processes in the aquifer such as precipitation and when corrosion plates block pore space. Additionally, biological reactions can either directly affect the physical flow structure (biofilm) or trigger chemical reactions (triggered precipitation or corrosion). We can consider these effects in terms of particulate matter that occludes natural grain-scale flow channels in a medium with spatially correlated poroperm properties as illustrated in Figure 4.

Power-law scaling porosity distribution overprints the horizontal geological layering of the aquifer in Klaipeda similar to observations in many geological environments all around the world [25]. The same spatial correlations exist laterally along the aquifer. The importance of these spatial correlations can be seen in part by noting that uncorrelated spatial well-log fluctuations have a flat or white noise spectrum. However, power spectra of the porosity well logs show that the Klaipeda sedimentary sequence is spatially correlated over two orders of magnitude in scale length (m-Hm) (Figure 4). Spectral scaling systematics in crustal well logs extends the observed range of scaling relations of porosity for five orders of magnitude. Spatial correlation extending to the grain scale means that few large-scale high permeable pathways control the fluid flow in the general crust (e.g., [1]). We discuss how applying the spatial correlation phenomenology to the connection of injection borehole to the formation results in exponentially declining injectivity curves (Figure 6).

Following a flow modelling method in the Appendix, explicit modeling of flow clogging in spatially correlated versus spatially uncorrelated poroperm media illustrates this exponential injectivity decline behavior. Figure 6(a) shows a model fit to injectivity decline at Klaipeda assuming fluid flow in a spatially correlated poroperm medium. Figure 6(b) contrasts Figure 6(a) exponential curve with a best fit to fluid flow in a medium having a spatially uncorrelated poroperm flow structure. The quasilinear best fit decline curve of Figure 6(b) is a poor fit to the observed Klaipeda injectivity decline. Such linear to quasilinear decline curves are regularly associated with "deep filtration" models of injectivity decline [26].

Accordingly, Figure 7 compares 2D wellbore models within spatially correlated and uncorrelated poroperm media

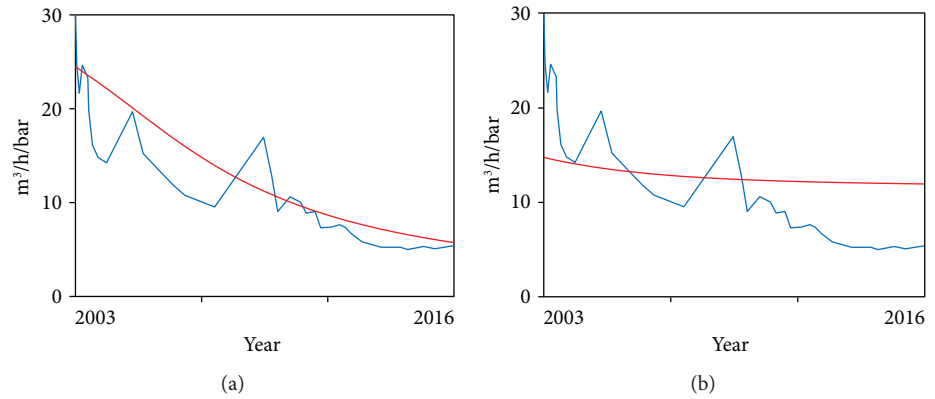

Figure 6: Observed and modeled decline curves for spatially correlated (a) and spatially uncorrelated (b) poroperm flow properties.

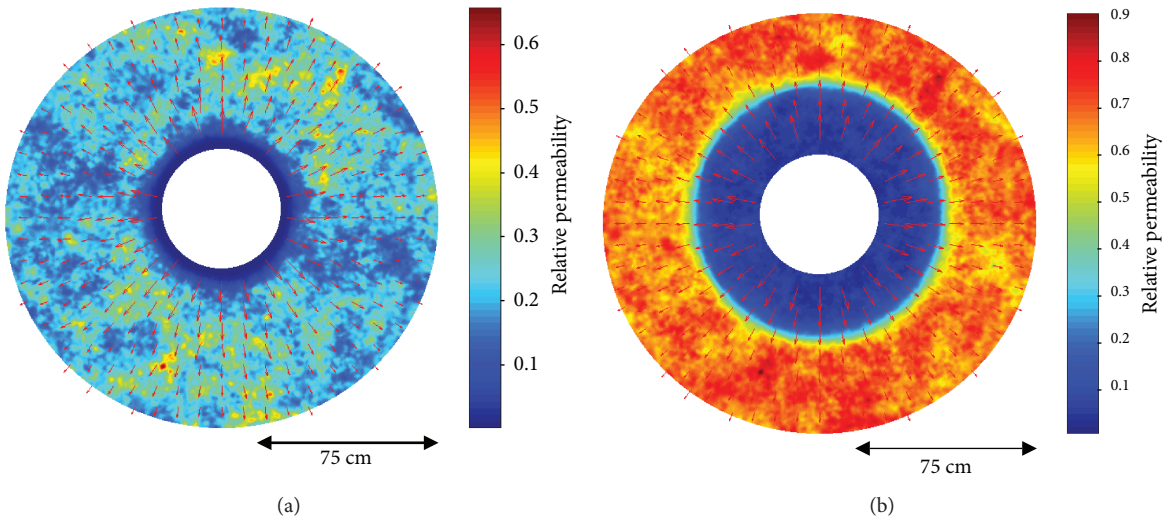

Figure 7: 2D wellbore model showing depth of penetration of wellbore occlusion damage for fluid flow in spatially correlated poroperm media (wellbore near skin effect, (a)) with spatially uncorrelated poroperm media (deep damage zone, (b)).

based on a power-law scaling permeability distribution. The occlusion is confined to the vicinity of the wellbore in the models, which is widely known as skin effect. For a spatially uncorrelated poroperm medium, the damage zone extends arbitrarily far into the poroperm medium surrounding the wellbore. Remediation of a near-wellbore skin effect is significantly more likely than remediation of flow damage extending far from the wellbore. This simulation reflects the results from this study in general. At the Klaipeda site, fines migration, precipitation, biofilm, and corrosion lead to a skin effect around the borehole and are the main causes for the exponential injectivity decline. Especially, their interaction results in reservoir-damaging effects as described in the following.

The large difference between productivity and injectivity in the same wells indicates a direction-dependent fluid barrier. Thus, when sucking water, the skin surrounding the wellbore is believed to detach from the reservoir and clears fluid pathways which are clogged during injection.

Microbial activity and the use of gypsum inhibitor is an example for the interaction between biological and chemical processes: the total microbial activity is measured in cell counts, which is ranked to be low (10^2 cells/ml) at the Klaipeda site. In contrast, microbial activity at other geothermal plants ranges from 10^3 to 10^7 cells/ml [27–29]. The total value at the Klaipeda site is lower at the production site (3.04 $*10^2$ cells/ml) compared to injection site (8.58$*10^2$ cells/ml). Thus, the natural environment at the Klaipeda site provides only small resources for the existence of organisms compared to artificially triggered microbial activity.

The natural DOC in water is low ranging around 2 mg C/l (increasing from production to injection site). H_2S can be caused by microbial activity [30]. At the Klaipeda site, it is only 0.0005% of total gas content. Therefore, the use of organic-based gypsum inhibitor, which is injected at the production wellhead, is presumably responsible for the microbial activity. Additionally, organic content is leached from surface filter installations. Hence, the microbial activity mainly develops due to surface infrastructure of the plant triggered by artificially introduced organic content. In later stages, microbial activity most probably leads to

the formation of biofilm, which has a direct impact on fluid flow pathways by clogging pores. To overcome this problem, bactericides have been injected at the production site. However, no long-term effect has been proven providing injectivity increase.

On the other hand, the use of gypsum inhibitor (4-5 mg/m^3) successfully prevents clogging of surface pipes since 2004. Condition of the pipelines has been checked by video inspection by the site operator in 2016. Before the use of gypsum inhibitor, massive gypsum precipitations had clogged the wells and surface infrastructure.

Hydrochemical modeling suggests precipitation of other minerals such as silica/clays and sulfate minerals, which are also accumulated in filter residual. Especially, during the standby of the power plant in summers, the possibility of mineral precipitation is increased. Furthermore, element concentrations in water increase due to mineral dissolution in the aquifer. Especially, the increase of HCO_3 indicates the dissolution of the carbonatic sandstone matrix. The dissolution of carbonates and fine particles is enhanced by acidation. Additionally, acidation can damage the aquifer formation containing aluminosilicates by dissolving aluminum and forming hydrated silica [31]. Acid stimulation is also known to trigger clay mobilization [32]. Clay particles later block pores in sandstones. The best acid formulation preventing precipitation is selected using simulators [33].

In Klaipeda, Fe and Mn concentrations increase especially from the production to injection sites. This is an indicator for corrosion in wells and surface pipes in both sites. At injection wells, corrosion is additionally triggered by acidation treatments. However, correlation of Mn, Fe, and Si shows that corrosion also occurs at the production site and in pipelines. Indeed, analysis shows that 60% of solid filter residual is related to corrosion.

Physical properties of the aquifer can cause negative effects on fluid flow. At the Klaipeda site, pores in sandstone have the size of clay and silt particles (3–40 μm). The interlayering of clay and sandstones is favorable for clay particle movement. During injection, clay particles can completely block the pores in sandstones. Additionally, the poor cementation of sandstone favors a leaching of matrix particles especially during acidation. If a pumping test is not performed after acidation, dissolved particles remain in the aquifer and block pores during injection phases. During production phase, these particles are removed causing high productivity indices.

The variety of reasons for injectivity decrease at the Klaipeda site mentioned above are typical mechanisms for injectivity decrease in clastic sedimentary aquifers. Additional problems can occur, that is, caused by temperature-related precipitations or flow velocities [34]. Nevertheless, our study shows that changes of physical, chemical, and biological properties in the aquifer causing injectivity problems are visible in the field data at an early stage. Corrosion particles and precipitated minerals accumulate in surface filters, and their size can easily be compared with the pore radius of the aquifer formation. Changes in element concentrations or microbial cells can be directly measured at water samples taken from different locations at the geothermal cycle.

A risk of pore clogging should be determined as early as possible enhancing the chance of avoiding aquifer degradation. A feedback adjustment procedure can support the implementation of impeding treatments aiming for a sustainable use of geothermal aquifers [35].

6. Conclusion

The Klaipeda geothermal field faces decreasing injectivities while productivities from these wells are remarkably higher. Results of this study indicate that the Klaipeda aquifer is characterized by spatially correlated permeability structures. Only few highly permeable pathways control the main fluid flow in the aquifer. These permeable structures are blocked by particles originating from field operations, and therefore, injectivity drops rapidly leading to a wellbore near damage zone.

In particular, field operations cause changes of the physical, chemical, and biological processes in the aquifer. Chemical processes observed at the Klaipeda site are mainly mineral precipitation and corrosion. This study shows that especially cross-correlation of chemical elements and its strength analysis are feasible to cluster different element groups which respond to similar chemical reactions. These reactions are confirmed by sample analysis and hydrochemical modeling. Microbial activity at the site could cause biofilm formation. Repeated cell counting shows decreased activity over time. Additionally, leaching experiments with filter materials demonstrated the release of organic material from power plant equipment which might cause increased microbial activity at injection site. Analysis of physical boundary conditions and filter residual at the site determined fines migration from the reservoir. Moreover, physical, chemical, and biological processes can affect each other and generate further reactions. In Klaipeda, for example, microbial activity triggers corrosion in surface pipelines.

This study shows that reasons for pore clogging should be understood as early as possible to avoid long-term aquifer degradation. However, our results show that field data already allow verifying potential risks at early stages. Especially, the interaction of physical, chemical, and biological processes is important to consider, for example, microbiologically triggered corrosion. Our results show that spatially correlating nature of permeable structures is responsible for exponentially declining injectivity curves.

Appendix

A. 2D Wellbore-Centric Radial Injectivity Flow Decline Modelling into Spatially Correlated and Spatially Uncorrelated Flow Structures

Figure 7 illustrates the potential roles that spatially correlated versus spatially uncorrelated aquifer flow structures play in the observed Klaipeda injectivity decline process. We here outline the 2D injectivity decline flow modelling procedure.

Wellbore-centric fluid flow simulation in 2D computes a planar Darcy fluid velocity field $v(x, y)$ subject to constant pressure P boundary conditions at an internal wellbore radius and external far-field radius,

$$v(x, y) = \frac{\kappa(x, y)}{\mu} \nabla P(x, y), \quad (A.1)$$

for a fluid of viscosity μ in a model permeability field $\kappa(x, y)$. A computational grid is shown in Figure 8.

The permeability field $\kappa(x, y)$ is determined by the flow-layer porosity field $\varphi(x, y)$,

$$\kappa(x, y) = \kappa_0 \exp(\alpha\varphi(x, y)), \quad (A.2)$$

where α is a constant. For a normal distribution of porosities $0 < \varphi(x, y) < 1$, if $\alpha < \sim 3$, the associated permeability field is normally distributed, whereas if $\sim 15 < \alpha < \sim 35$, the permeability field is lognormally distributed. When, as indicated in the body of the text, the porosity field is spatially correlated, the associated permeability fields are only weakly correlated for $\alpha < \sim 3$ but are strongly correlated for $\sim 15 < \alpha < \sim 35$. The value of α determined from well core in hydrocarbon field worldwide is of order $\sim 15 < \alpha < \sim 35$, that is, crustal reservoir flow is observed worldwide to be both spatially correlated and lognormally distributed. Figure 7 illustrates these spatial correlation effects.

We are interested in circumstances in which small amounts of debris from the wellbore enter into the flow spatially correlated permeability flow channels and begin to occlude the channels. To simulate this occlusion process, we allow the value of α to vary with time and space, α where index n denominates an iterative time step from an initial state $\alpha_0 = constant$ to a final state $\alpha_n(x, y)$, which can vary according to the grid location (x, y). If at iterative step n, the grid location fluid velocity $v_n(x, y)$ is above a threshold velocity v_{thresh}, it is assumed that the fluid is moving fast enough to transport an occlusion particle, and the value of α at (x, y) is decremented, $\alpha_n(x, y) \to f \cdot \alpha_n(x, y)$, $f < 1$, as if the occlusion particle lodged in the grain-scale connectivity channel through which the fluid was passing. If the fluid velocity at (x, y) is below the threshold velocity, it is assumed that no occlusion particle is being transported, and $\alpha_n(x, y)$ remains unchanged.

The modelling process then proceeds to match a model injectivity decline curve derived from fitting an exponential decay curve to the observed Klaipeda injectivity declines. The model decline curve is modelled by a parameter search in which the threshold velocity v_{thresh} parameter and the α decrement factor f are varied to produce a series of iterative trial decline curves until the computed decline curve optimally matches the observed curve.

The curve fitting process is then run for a sequence of values of α_0 in order to see if the modelling process can fit suitable parameter pairs (f, v_{thresh}) to fit to the observed Klaipeda decline curves.

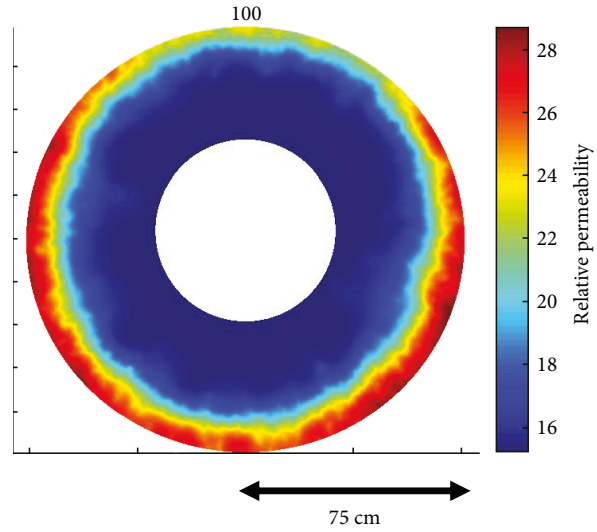

Figure 8: 2D Darcy flow simulation grid for computing wellbore-centric velocity variations due to spatially correlated porosity distributions documented in Figure 4 for Klaipeda geological sections. The above-illustrated flow simulation shows the case for low-poro-connectivity parameter $\alpha \sim 3$ characteristic of the "deep filtration" assumption for particulate transport. In the present simulation particulates are transported arbitrarily distances into the surrounding rock. If the poro-connectivity parameter is given values in the range $15 < \alpha < 30$ widely observed in hydrocarbon reservoirs, then particulate transport is confined to the vicinity of the wellbore because most active flow channels become clogged with particulates; this case is illustrated in Figure 7(a). Figure 6 indicates that observed exponential injector decline at Klaipeda is consistent with near-wellbore occlusion rather than deep filtration occlusion.

We find that

(i) for $\sim 15 < \alpha_0 < \sim 35$, it is straightforward for model decline curves to match the observed exponential decline curves;

(ii) for $\alpha_0 < \sim 3$, no (f, v_{thresh}) parameter pairs provide decline curves that match the observed exponential decline;

(iii) for $\sim 15 < \alpha_0 < \sim 35$, the majority of the decline curve occlusion process occurs in the vicinity of the wellbore;

(iv) for $\alpha_0 < \sim 3$, the decline curve occlusion occurs throughout the model radius as a steady growth of the occlusion zone.

From the last of the above model findings, it appears that the $\alpha_0 < \sim 3$ case of spatially uncorrelated flow connectivity effectively duplicates the standard assumption of "deep filtration" processes commonly used to model wellbore injectivity declines [25]. The first two above model findings suggest, however, that the "deep filtration" processes do not properly reflect the nature of crustal flow at the reservoir scale. If this proves to be that case—that wellbore injectivity declines do not proceed by "deep filtration" processes in spatial

uncorrelated poroperm flow media—then there may be useful remediation strategies that focus on near-wellbore treatment of occluded material.

Data Availability

The data used to support the findings of this study are available from the corresponding author upon request.

Conflicts of Interest

The authors declare that there is no conflict of interest regarding the publication of this paper.

Acknowledgments

The authors acknowledge the continuous support to the team of the section Geothermal Energy Systems at GFZ-Potsdam and GTN-Neubrandenburg. The authors thank Geoterma for the permission to publish this paper and the continuous support during site visits. The authors thank Saulius Sliaupa for the scientific discussions and hosting at the core storage. The authors appreciate the support of several labs at GFZ; S. Tonn, A. Vieth-Hillebrand, and K. Günther for the fluid analyses; A. Schleicher and C. Cunow for the geochemical rock analyses; and T. Scheytt and S. Rautenberg for the CNS analysis at TU-Berlin. M. Zimmer did the gas analysis, and C. Andermann supported the particle size analysis in fluids with equipment and analysis in the SedLab at GFZ-Section 5.1. The authors sincerely thank Mashal Alawi for doing the cell counting in water samples. The porosity measurements were performed with the use of the instruments provided by GFZ-Section 4.2. The DESTRESS project has received funding from the European Union's Horizon 2020 research and innovation program under Grant agreement no. 691728.

References

[1] P. Leary, P. Malin, and R. Niemi, "Fluid flow and heat transport computation for power-law scaling poroperm media," *Geofluids*, vol. 2017, Article ID 9687325, 12 pages, 2017.

[2] C. E. Neuzil, C. Cooley, S. E. Silliman, J. D. Bredehoeft, and P. A. Hsieh, "A transient laboratory method for determining the hydraulic properties of "tight" rocks-II. Application," *International Journal of Rock Mechanics and Mining Sciences*, vol. 18, no. 3, pp. 253–258, 1981.

[3] D. L. Gallup, "Iron silicate scale formation and inhibition at the salton sea geothermal field," *Geothermics*, vol. 18, no. 1-2, pp. 97–103, 1989.

[4] D. L. Gallup, "Aluminum silicate scale formation and inhibition: scale characterization and laboratory experiments," *Geothermics*, vol. 26, no. 4, pp. 483–499, 1997.

[5] P. Pryfogle, "Monitoring biological activity at geothermal power plants," Tech. Rep. INL/EXT-05-00803, Idaho National Laboratory (INL), Idaho Falls, ID 83415, USA, 2005.

[6] I. Matsunaga, H. Kobayashi, S. Sasaki, and T. Ishida, "Studying hydraulic fracturing mechanism by laboratory experiments with acoustic emission monitoring," *International Journal of Rock Mechanics and Mining Sciences & Geomechanics Abstracts*, vol. 30, no. 7, pp. 909–912, 1993.

[7] M. D. Zoback, F. Rummel, R. Jung, and C. B. Raleigh, "Laboratory hydraulic fracturing experiments in intact and pre-fractured rock," *International Journal of Rock Mechanics and Mining Sciences*, vol. 14, no. 2, pp. 49–58, 1977.

[8] D. L. Gallup, "Aluminum silicate scale formation and inhibition (2): scale solubilities and laboratory and field inhibition tests," *Geothermics*, vol. 27, no. 4, pp. 485–501, 1998.

[9] G. Stáhl, G. Pátzay, L. Weiser, and E. Kálmán, "Study of calcite scaling and corrosion processes in geothermal systems," *Geothermics*, vol. 29, no. 1, pp. 105–119, 2000.

[10] O. Kolditz, S. Bauer, L. Bilke et al., "OpenGeoSys: an open-source initiative for numerical simulation of thermo-hydro-mechanical/chemical (THM/C) processes in porous media," *Environment and Earth Science*, vol. 67, no. 2, pp. 589–599, 2012.

[11] K. Pruess, "Modeling of geothermal reservoirs: fundamental processes, computer simulation and field applications," *Geothermics*, vol. 19, no. 1, pp. 3–15, 1990.

[12] M. G. Blöcher, G. Zimmermann, I. Moeck, W. Brandt, A. Hassanzadegan, and F. Magri, "3D numerical modeling of hydrothermal processes during the lifetime of a deep geothermal reservoir," *Geofluids*, vol. 10, no. 3, pp. 406–421, 2010.

[13] M. Brehme, G. Blöcher, M. Cacace, Y. Kamah, M. Sauter, and G. Zimmermann, "Permeability distribution in the Lahendong geothermal field: a blind fault captured by thermal–hydraulic simulation," *Environmental Earth Sciences*, vol. 75, no. 14, p. 1088, 2016.

[14] J. Taron and D. Elsworth, "Thermal-hydrologic-mechanical-chemical processes in the evolution of engineered geothermal reservoirs," *International Journal of Rock Mechanics and Mining Sciences*, vol. 46, no. 5, pp. 855–864, 2009.

[15] C.-F. Tsang, "Coupled hydromechanical-thermochemical processes in rock fractures," *Reviews of Geophysics*, vol. 29, no. 4, pp. 537–551, 1991.

[16] S. Regenspurg, E. Feldbusch, J. Byrne et al., "Mineral precipitation during production of geothermal fluid from a Permian Rotliegend reservoir," *Geothermics*, vol. 54, pp. 122–135, 2015.

[17] F. Zinevicius, V. Rasteniene, and A. Bickus, "Geothermal development in Lithuania," in *Proceedings of the European Geothermal Conference, Szeged*, pp. 25–30, Hungary, 2003.

[18] C. Gerber, R. Vaikmäe, W. Aeschbach et al., "Using 81 Kr and noble gases to characterize and date groundwater and brines in the Baltic Artesian Basin on the one-million-year timescale," *Geochimica et Cosmochimica Acta*, vol. 205, pp. 187–210, 2017.

[19] M. Brehme, F. Deon, C. Haase et al., "Fault controlled geochemical properties in Lahendong geothermal reservoir Indonesia," *Grundwasser*, vol. 21, no. 1, pp. 29–41, 2016.

[20] M. Brehme, T. Scheytt, M. Çelik, and U. E. Dokuz, "Hydrochemical characterisation of ground and surface water at Dörtyol/Hatay/Turkey," *Environment and Earth Science*, vol. 63, no. 6, pp. 1395–1408, 2011.

[21] M. Börger, "Microbial diversity and abundance in the deep subsurface of the South-Eastern North German Basin and the Western Pannonian Basin, [M.S. thesis]," Potsdam University, 2017.

[22] F. Deon, H.-J. Förster, M. Brehme et al., "Geochemical/hydrochemical evaluation of the geothermal potential of

the Lamongan volcanic field (Eastern Java, Indonesia)," *Geotherm Energy*, vol. 3, no. 1, article 20, 2015.

[23] A. Mudroch, J. M. Azcue, and P. Mudroch, *Manual of Physico-Chemical Analysis of Aquatic Sediments*, CRC Press, 1996.

[24] P. C. Leary, "Fractures and physical heterogeneity in crustal rock," in *Heterogeneity of the Crust and Upper Mantle—Nature, Scaling and Seismic Properties*, J. A. Goff and K. Holliger, Eds., pp. 155–186, Kluwer Academic/Plenum Publishers, New York, NY, USA, 2002.

[25] P. Leary, P. Malin, P. Geiser, J. Pogacnik, J. Rugis, and B. Valles, "Flow lognormality and spatial correlation in crustal reservoirs–I: physical character & consequences for geothermal energy," in *Proceedings World Geothermal Congress 2015*, p. 9, Melbourne, Australia, April 2015.

[26] A. C. Alvarez, P. G. Bedrikovetsky, G. Hime, A. O. Marchesin, D. Marchesin, and J. R. Rodrigues, "A fast inverse solver for the filtration function for flow of water with particles in porous media," *Inverse Problems*, vol. 22, no. 1, pp. 69–88, 2006.

[27] D. G. Ellis, R. W. Bizzoco, and S. T. Kelley, "Halophilic archaea determined from geothermal steam vent aerosols," *Environmental Microbiology*, vol. 10, no. 6, pp. 1582–1590, 2008.

[28] H. Kimura, M. Sugihara, H. Yamamoto, B. K. C. Patel, K. Kato, and S. Hanada, "Microbial community in a geothermal aquifer associated with the subsurface of the great Artesian Basin, Australia," *Extremophiles*, vol. 9, no. 5, pp. 407–414, 2005.

[29] V. T. Marteinsson, S. Hauksdottir, C. F. V. Hobel, H. Kristmannsdottir, G. O. Hreggvidsson, and J. K. Kristjansson, "Phylogenetic diversity analysis of subterranean Hot Springs in Iceland," *Applied and Environmental Microbiology*, vol. 67, no. 9, pp. 4242–4248, 2001.

[30] D. Dinur, B. Spiro, and Z. Aizenshtat, "The distribution and isotopic composition of sulfur in organic-rich sedimentary rocks," *Chemical Geology*, vol. 31, pp. 37–51, 1980.

[31] S. L. Bryant and D. C. Buller, "Formation damage from acid treatments," *SPE Production Engineering*, vol. 5, no. 4, pp. 455–460, 1990.

[32] D. E. Simon and M. S. Anderson, "Stability of clay minerals in acid," in *SPE Formation Damage Control Symposium*, pp. 7–18, Lafayette, LA, USA, February 1991.

[33] M. P. Walsh, L. W. Lake, and R. S. Schechter, "A description of chemical precipitation mechanisms and their role in formation damage during stimulation by hydrofluoric acid," *Journal of Petroleum Technology*, vol. 34, no. 9, pp. 2097–2112, 1982.

[34] P. Ungemach, "Reinjection of cooled geothermal brines into sandstone reservoirs," *Geothermics*, vol. 32, no. 4–6, pp. 743–761, 2003.

[35] M. Brehme, G. Blöcher, S. Regenspurg, and E. Huenges, "Approach to develop a soft stimulation concept to overcome formation damage – a case study at Klaipeda, Lithuania," in *Proceedings, 42nd Workshop on Geothermal Reservoir Engineering*, pp. 1–5, Stanford, CA, USA, February 2017.